
Planted: a dataset for planted forest identification from multi-satellite time series

Luis Miguel Pazos-Outón*
Mineral AI

Cristina Nader Vasconcelos
Google DeepMind

Anton Raichuk
Google DeepMind

Anurag Arnab
Google DeepMind

Dan Morris
Google Research

Maxim Neumann
Google DeepMind

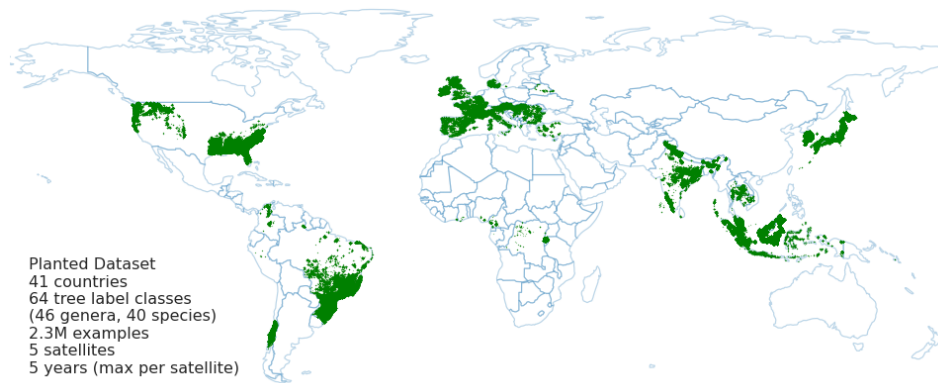


Figure 1: Overview of the *Planted* dataset and the geographical samples distribution.

Abstract

Protecting and restoring forest ecosystems is critical for biodiversity conservation and carbon sequestration. Forest monitoring on a global scale is essential for prioritizing and assessing conservation efforts. Satellite-based remote sensing is the only viable solution for providing global coverage, but to date, large-scale forest monitoring is limited to single modalities and single time points. In this paper, we present a dataset consisting of data from five public satellites for recognizing forest plantations and planted tree species across the globe. Each satellite modality consists of a multi-year time series. The dataset, named *Planted*, includes over 2M examples of 64 tree label classes (46 genera and 40 species), distributed among 41 countries. This dataset is released to foster research in forest monitoring using multimodal, multi-scale, multi-temporal data sources. Additionally, we present initial baseline results and evaluate modality fusion and data augmentation approaches for this dataset.

1 Introduction

Forests, covering a third of the Earth’s surface, are the most diverse and complex land cover type, and host over 80% of all terrestrial species. Forests also play a critical role in capturing atmospheric carbon: current estimates suggest that deforestation and land degradation cause 11% of current carbon emissions, and forest-based solutions can provide 27% of the mitigation needed to achieve Paris

*This work was done while contributing at Google DeepMind.

agreement targets, with an annual mitigation potential of 4 gigatons of CO₂-equivalent emissions per year by 2030 Programme (2022).

Global monitoring of forests is a promising path to understand the global rates of carbon fluxes and the effectiveness of biodiversity conservation efforts. Remote sensing provides frequent, high-resolution, global imagery, and thus offers a plausible path to global forest monitoring. However, with global coverage comes a significant data review burden that often exceeds the capacity of the conservation community. AI tools are therefore required to fully realize the potential of remote-sensing-based forest understanding. Fortunately, advances in computer vision have been transferred to the remote sensing domain with significant success for detecting forest cover loss and gain Hansen *et al.* (2013), estimating forest canopy height Tolan *et al.* (2023), and even estimating the carbon content of individual trees Tucker *et al.* (2023) at regional to global scales.

At the same time, remote sensing of the Earth's surface from satellite imagery poses its own challenges. Satellite coverage is not uniform around the world, with many temporal, spectral, and geographical data gaps. Different satellite instrument types are sensitive to different forest properties. Data quality and coverage can vary significantly even for individual data sources. Consequently, no single satellite source can provide a complete picture of forest composition, necessitating multi-satellite solutions.

In this work, we construct a planted tree dataset based on a curated subset of the "Spatial Database of Planted Trees" Harris *et al.* (2019), extended with several satellite imagery modalities across long time series. Planted forests are regions of planted trees that will be harvested for timber or wood fiber products, and tree crops are regions of planted trees from which products are harvested without removing the trees, for example palm oil, fruit, rubber, and coffee². As of 2015, about 173 million hectares (4% of total tree cover) were covered by planted forests, and about 50 million hectares by tree crops Harris *et al.* (2019), though the accurate localization of planted forests and tree crops is not possible yet. This dataset offers a challenge for the community to develop approaches to recognize *planted forests* and *tree crops*.

With this work, we aim to foster AI research in remote sensing of forests using multimodal data sources. Our main contributions are: A curated multimodal dataset for planted forest and tree crop recognition, initial baselines results with a simple multimodal multi-temporal transformer model, and preliminary evaluation of data fusion and data augmentation approaches.

2 Background

Remote sensing of forests uses a range of instrument types: optical, multi-spectral, hyper-spectral, synthetic aperture radar (SAR), and lidar Elachi & Van Zyl (2006). These instruments also span a range of spatial resolutions, centimeter scale to kilometer scale. Each instrument and resolution offers a view into different elements of forest composition.

High-resolution optical imagery (30cm to several meters per pixel) has been used, for example, to identify free-standing trees on a regional scale, and to estimate properties related to tree canopy extent, height, and biomass Tucker *et al.* (2023); Tolan *et al.* (2023). Multi-spectral imagery, usually providing regular time series at medium resolution (10 to 30 meters per pixel), is frequently used for analyzing forest loss and gain Hansen *et al.* (2013) or forest type classification. Hyperspectral imagers provide more and narrower spectral bands, enabling the analysis of fine forest characteristics related to forest health or species composition. Synthetic aperture radar (SAR) and lidar are active sensors, emitting their own electromagnetic waves and measuring the scattered signal from the surface. SAR in particular, due to the use of long wavelengths, is nearly independent of time of day and can penetrate clouds, rain, and parts of the forest canopy. In particular polarimetric and interferometric SAR is sensitive to 3D forest structure and moisture content, and is used for change/anomaly detection, forest type classification, and biomass estimation Papathanassiou *et al.* (2021). Lidar can provide very fine vertical distributions of scattering elements within a small area, and thus can be used to reconstruct the vertical profile of the forest Potapov *et al.* (2021).

²In the following we will use the term *forest plantation* or just *plantation* to imply both forest timber plantations and tree crop plantations.

3 Related work

3.1 Remote sensing datasets for machine learning

The application of deep learning to remote sensing data has primarily focused on high-resolution optical imagery, which has similar characteristics to the natural images that are widely used in computer vision research. Therefore many public remote sensing datasets consist primarily of high-resolution optical imagery (e.g. UC Merced Yang & Newsam (2010) or FMoW Christie *et al.* (2018)). The Sentinel-2 satellite program is the highest-resolution publicly-available optical satellite imagery, with 10m pixel resolution and a revisit time of approximately five days. Consequently, numerous land cover classification datasets have focused on Sentinel-2 data, for example EuroSAT Helber *et al.* (2019), BigEarthNet Sumbul *et al.* (2019), or Dynamic World Brown *et al.* (2022). Optical and multi-spectral satellite imagery are often combined with non-optical imagery, such as SAR data from the Sentinel-1 program, for example So2SAT Zhu *et al.* (2020), Sen12 Schmitt *et al.* (2018), LandCoverNet Alemohammad & Booth (2020), and CropHarvest Tseng *et al.* (2021). These datasets have broad geographic coverage, but do not provide the granularity of forest categories required to advance forest characterization models.

Forest-specific remote sensing datasets include ReforesTree Reiersen *et al.* (2022), which provides labeled drone imagery over Ecuador; TreeSatAI Schulz *et al.* (2022), which combines Sentinel-1/2 and aerial imagery over a forest region in Germany; and the MultiEarth challenge, which combines imagery from the Sentinel-1, Sentinel-2 and Landsat 8 satellites over the Amazon forest Cha *et al.* (2022) with forest segmentation masks. These datasets are specific to forests, but provide narrow geographic coverage and lack category labels that would facilitate the identification of planted forests.

3.2 Transformers and data fusion

Transformers, initially introduced for language modeling Vaswani *et al.* (2017), have been extended to images Kolesnikov *et al.* (2021), video Arnab *et al.* (2021), and audio Gong *et al.* (2021). Transformers can naturally be applied to different modalities, since they operate on sequences of abstract tokens. Examples of multimodal fusion with transformers include combining image and text for captioning and visual question answering Lu *et al.* (2019); Li *et al.* (2019); Wang *et al.* (2022), or combining audio and visual information Nagrani *et al.* (2021); Georgescu *et al.* (2022); Jaegle *et al.* (2021) among others. In the remote sensing domain, Garnot *et al.* Sainte Fare Garnot *et al.* (2022), for example, evaluated data fusion approaches of Sentinel-1 and Sentinel-2 data for crop type monitoring, where they introduced a variant of the U-Net Ronneberger *et al.* (2015) model with temporal attention.

4 The *Planted* Dataset

The *Planted* dataset³ is constructed to assess the potential to recognize different types of planted forests and tree crops from diverse satellite data sources. It is a unique, global, multimodal, multi-temporal, multi-scale classification dataset that encourages the development of methods for sensor fusion and time series modeling for forest monitoring applications. Each example contains satellite imagery, labels, and metadata. We create dense imagery cubes for each modality, to cover exactly the same area on the ground at specified date ranges. See Table 1 for the types and dimensions of all features included in each example.

4.1 Satellite data

Each data example contains image patches across time for the five satellite data sources covering an area of 120 meters x 120 meters. Due to differing resolutions among the satellites, the actual image sizes (height and width) vary from satellite to satellite. Additionally, each satellite modality has a different number of time series samples and bands. Table 2 provides an overview of the sample dimensions, pixel resolution, and temporal characteristics per satellite.

³The dataset is released under the Creative Commons Attribution 4.0 International (CC-BY-4.0) license, and is available at <https://storage.googleapis.com/planted-datasets/public> (version 1.0.1).

Table 1: List of features in each example in our dataset.

Satellite data			
<i>name</i>	<i>type</i>	<i>dimensions</i>	<i>description</i>
s1	float	(8,12,12,3)	Sentinel-1 backscatter & look angle
s2	int	(8,12,12,10)	Sentinel-2 reflectivity
l7	int	(20,4,4,6)	Landsat-7 reflectivity
modis	float	(60,1,1,7)	MODIS reflectivity & derivatives
alos	float	(4,4,4,3)	ALOS PALSAR backscatter & look angle
s1_timestamps	int	(8)	Sentinel-1 timestamps
s2_timestamps	int	(8)	Sentinel-2 timestamps
l7_timestamps	int	(20)	Landsat 7 timestamps
modis_timestamps	int	(60)	MODIS timestamps
alos_timestamps	int	(4)	ALOS PALSAR timestamps
s1_mask	int	(8,12,12,3)	Sentinel-1 mask
s2_mask	int	(8,12,12,10)	Sentinel-2 mask
l7_mask	int	(20,4,4,6)	Landsat 7 mask
modis_mask	int	(60,1,1,7)	MODIS mask
alos_mask	int	(4,4,4,3)	ALOS PALSAR mask

Labels			
<i>name</i>	<i>type</i>		<i>description</i>
common_name	string		Common name of the tree species
species	string		Species name
conifer_broad	string		Whether conifer or broad-leaf
ever_dec	string		Whether evergreen or deciduous
hard_soft	string		Whether hard or soft wood

Metadata			
<i>name</i>	<i>type</i>	<i>unit</i>	<i>description</i>
country	string		Country name
area_ha	float	ha	Area of forest plot, in hectares
perimeter_km	float	km	Perimeter of forest plot, in kilometers
elevation	float	m	Elevation above sea surface, in meters
lat	float	deg	Latitude, in degrees
lon	float	deg	Longitude, in degrees

Table 2: Satellite data characteristics. Columns: Satellite name, abbreviation, instrument type, resolution in meters, frequency of data collection, time range for temporal aggregation, start of time series, tensor dimensions in each example (T,H,W,C) = (time series samples, height, width, number of channels).

Satellite	Instrument	Res.	Frequency	Temporal agg.	Time range	Start	Dimensions
Sentinel-1	SAR C-band	10m	5 days	seasonal	2 years	01/2016	(8,12,12,3)
Sentinel-2	Multi-spectral	10m	5 days	seasonal	2 years	01/2016	(8,12,12,10)
Landsat 7	Multi-spectral	30m	16 days	seasonal	5 years	01/2013	(20,4,4,6)
ALOS-2	SAR L-band	30m	6-30 days	yearly	3 years	01/2015	(4,4,4,3)
MODIS	Multi-spectral	250m	daily	monthly	5 years	01/2013	(60,1,1,7)

Satellite data for each example contains a multi-year time series. The start and end times of the time series within an example are not the same for all satellites due to different start times and duration of data acquisition. To reduce the data size, we aggregate images based on satellite-specific temporal reduction functions. Temporal reductions can be monthly, seasonal (i.e. 3 months), or yearly. MODIS and Landsat 7 have full data coverage over the time range (2013-2017), while others do not due to later satellite launches and data availability. Some examples have missing images due to having missing or low-quality filtered-out data. This is a common issue when dealing with remote sensing data, either due to meteorological, geographical, or instrument-specific constraints. The satellite-dependent temporal distribution of invalid samples is presented in the supplementary material.

For each satellite image source and each time sample we added timestamps (mean of the time range) as an integer, counting the number of milliseconds since *1970-01-01T00:00:00Z*. For convenience, we included date strings in the format *YYYY-MM-DD*. Finally, each image patch is accompanied by a binary mask of pixel validity.

The following imaging instruments are included in the *Planted* dataset:

- Sentinel-1 (S1): Synthetic aperture radar (SAR) providing data since 2014.
- Sentinel-2 (S2): Multispectral satellite providing data since 2015.
- Landsat 7 (L7): Multispectral satellite imagery, provided data from 1999 to 2022.
- ALOS-2 (Advanced Land Observing Satellite) PALSAR-2: Synthetic aperture radar (SAR), providing data since 2014.
- MODIS (Moderate Resolution Imaging Spectroradiometer): Medium resolution multispectral satellite imagery, providing data since 1999.

For more details about satellite characteristics and individual bands, see the supplementary material.

4.2 Labels

The *Planted* dataset consists of 64 forest and plantation tree classes, from 41 countries, and a total of 2,264,747 examples. The geographic distribution of samples is shown in Figure 1. Each example includes the common name class (64), genus (46), and, when known, the tree species (40). The labels are based on a subset of Harris *et al.* (2019), having been curated as described in subsection 5.1. The approximate years of data labeling are 2013-2015, though the exact time associated with each label is not known. In addition to the tree species, the categorization into broad-leaf vs. conifer, evergreen vs. deciduous, hard- vs. soft-wood, and planted trees vs. tree crops are provided.

The dataset is unbalanced, with numbers of examples for a given class ranging between 15 and 450k. In order to facilitate more reliable evaluation, we introduce a frequency annotation to each species label. Categories with less than 200 samples are assigned to the *rare* sub-split, categories with ≥ 200 and $< 10k$ samples are assigned to the *common* sub-split, and those with $\geq 10k$ are assigned to the *frequent* sub-split. All species and their frequency annotations are listed in the Appendix.

4.3 Metadata

Additional metadata about the forest plantations includes the country, the area of the plantation in hectares, the perimeter of the plantation, the elevation in meters, and the center latitude and longitude in degrees.

4.4 Examples analysis

The temporal signatures of MODIS spectral bands and derived indicators for ten randomly selected tree species are shown in Figure 2. The date range covers the years from 2013 to 2016. Each band is normalized to have a mean of 0 and a standard deviation of 1. It illustrates and emphasizes the importance of temporal and spectral signatures for forest monitoring – the signatures differ significantly among tree species and correlate with seasonality.

5 Methods

5.1 Dataset generation

The labels are based on the Spatial Database of Planted Trees (v1.0) Harris *et al.* (2019). We performed an extensive analysis of the provided data and selected a subset of the examples for the first version of the *Planted* dataset based on the following criteria:

1. We explicitly filtered out examples which have been labeled by another machine learning approach — in order not to distill a potentially weaker model. The source labels should be based on manual labeling or surveys.

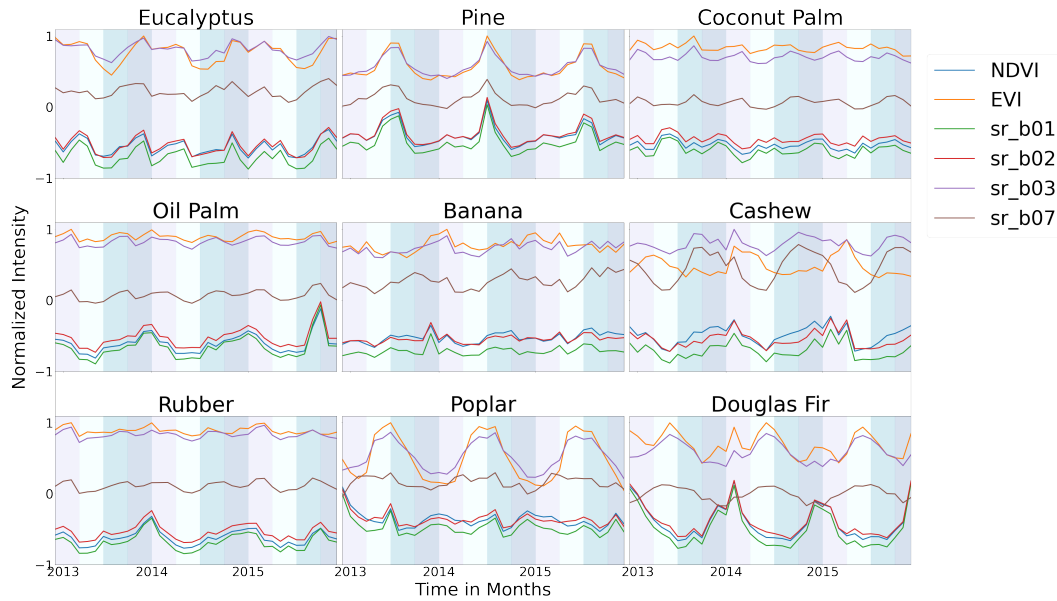


Figure 2: Temporal signatures of randomly selected tree species across MODIS spectral reflectance bands and NDVI and EVI indicators.

2. The species information should be known exactly. We keep only monoculture forest plantations and drop mixtures or poorly defined species examples.
3. The minimum area of forest plantation should be at least one quarter of a hectare.
4. We de-duplicated samples locations to be at least 70m from each other.
5. After those steps, the final filter included dropping species with less than 10 examples.

This resulted in a global dataset, consisting of 64 forest and plantation tree species, from 41 countries, and a total of 2,264,747 examples.

For satellite data processing and extraction of the localized regions of interest (ROIs), we used Google Earth Engine Gorelick *et al.* (2017). The following processing steps were performed:

1. Constructing deterministic data ranges for individual satellite data (yearly for ALOS, monthly for MODIS, and seasonally for Sentinel-1/2 and Landsat 7).
2. Filtering out bad data (e.g. based on cloud cover).
3. Spatial re-sampling of all bands at satellite-dependent nominal resolution.
4. Adding a mask for invalid pixels or invalid images.
5. Aggregation of multiple samples within a given date range into a single multi-band image: The reduce function for Sentinel-1, ALOS, MODIS was the *mean*, while for Sentinel-2 and Landsat 7 it was a *cloud-coverage-based mosaic*.
6. Extraction of resolution-dependent multi-band images with a size of 120 meters x 120 meters centered at the forest plantation center.

The examples were distributed into three splits (*train, validation, and test*), with a reference ratio of 8:1:1, respectively. However, to ensure reliable evaluation, for classes with less than 100 total examples, we used a 1:1:1 ratio, and we limited the number of validation and test examples to about 1000. We used an adaptive *geographic splitting* approach, first dividing the world into regions of approximately 20x20 km (400 km²) to 80x80 km (6400 km²) (depending on how many such regions we got per label), and assigning all samples within one such region randomly to one of the three splits. The distribution of labels across the splits is available in the Appendix.

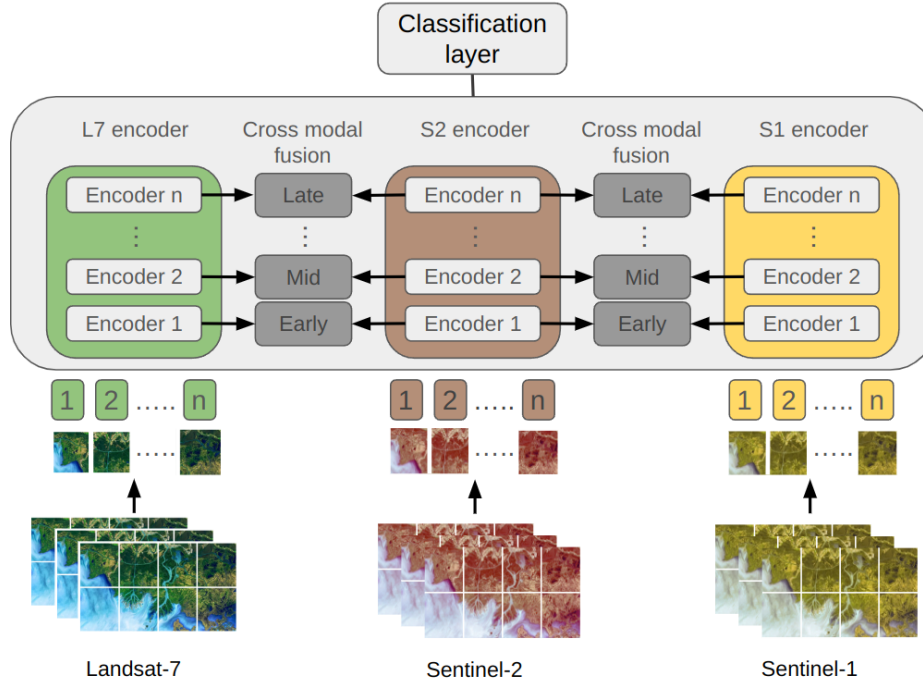


Figure 3: Depiction of the multimodal transformer architecture. In early fusion all cross-modal layers are activated, in mid fusion the early layers are excluded and we rely on the mid layer and the final layers. In late fusion only the last cross-modal layers are used.

5.2 Transformer model

Transformers are generic architectures based on non-local attention mechanism that operate on any sequence of tokens. Vision transformers Kolesnikov *et al.* (2021) obtain tokens by linearly projecting non-overlapping, 2D patches from the input image. Transformer models for video Arnab *et al.* (2021) extend the tokenization process to 3D patches (or *tubelets*) in order to include the temporal axis, as conceptually visualized in Figure 3.

In this dataset, most satellites contain both spatial and temporal dimensions, and we therefore tokenize them with 3D patches. The exception to this is MODIS, for which each pixel is larger than the patch size, so MODIS can be seen as a 1D time series which is tokenized with a 1D patch.

5.3 Multimodal fusion

Straightforward approaches for fusing multiple modalities include *early fusion* and *late fusion*. In *early fusion*, we extract tokens from each modality, concatenate them, and process them with a transformer. *Late fusion*, in contrast, processes each modality with a separate model. Tokens from each modality are then concatenated together before being passed to a linear classifier.

Early fusion Karpathy *et al.* (2014) is simple, but computationally expensive, as the sequence length increases linearly with the number of modalities, and computation in transformers has quadratic complexity with respect to the number of tokens.

Late fusion is practical, as it allows us to re-use models already trained for a single modality Karpathy *et al.* (2014); Simonyan & Zisserman (2014). The number of model parameters, however, grows linearly with the number of modalities.

Mid fusion Nagrani *et al.* (2021); Sainte Fare Garnot *et al.* (2022) strikes a balance between *early* and *late fusion*, by initially processing modalities independently of one another, before fusing them at an intermediate point in the network.

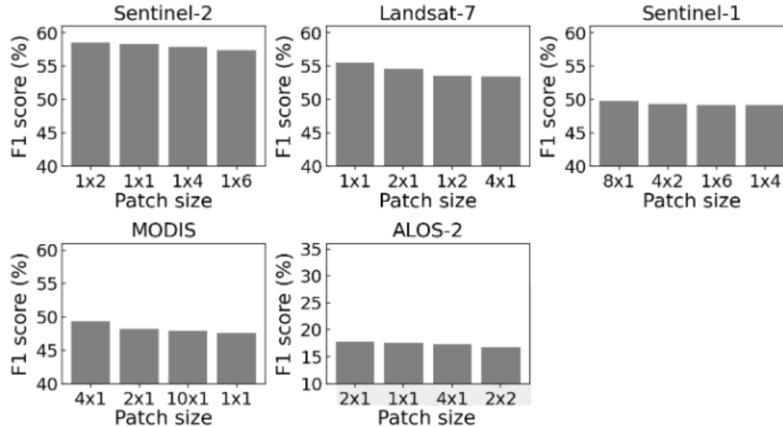


Figure 4: Patch size ablations for each satellite. The best patch size is satellite-dependent. The notation above refers to time x spatial dimensions.

6 Experimental results

6.1 Experimental setup

For the initial baseline experiments we used a standard vision transformer Kolesnikov *et al.* (2021) architecture extended to multi-temporal 3D data inputs as in video Arnab *et al.* (2021). Our default baseline transformer encoder architecture contains 12 layers with three self-attention heads, with an embedding size of 192 and an MLP size of 768. Pre-processing consists of per-modality input data normalization using robust statistics in order to minimize the effect of outliers, which are common in remote sensing data (median for center and median absolute deviation (MAD) for scale). Optionally, data augmentations during training are performed as described in the experiments below. By default, we use the Adam optimizer with a learning rate of 0.001 and weight decay of 0.0001, minimizing the softmax cross-entropy loss.

We evaluate the performance using the *overall accuracy* and the *macro F1 score* metrics, which we report for the entire split. We further break down the F1 metrics into *rare*, *common*, and *frequent* sub-splits. The overall accuracy is micro-averaged, considering each example independently. The F1 score is macro-averaged across the classes. It is defined as:

$$F1 = \frac{1}{C} \sum_c \frac{2TP_c}{2TP_c + FP_c + FN_c} \quad (1)$$

where C is the number of classes, and TP_c , FP_c , FN_c are the true positives, false positives, and false negatives of class c . For reporting F1 on label frequency sub-splits, we average per-class $F1_c$ over the set of labels in the *rare*, *common*, and *frequent* categories.

6.2 Embedding patch sizes

In the first series of experiments, we explore performance of basic transformers using only a single satellite data modality. Since the spatio-temporal image sizes vary significantly among satellites, we first investigate different patching strategies. Figure 4 shows the performance of different patch sizes. A patch size, denoted as $T \times S$, implies a 3D patch of temporal size T , and spatial height and width sizes S . As we can see, for the current model configuration and processing, the optimal patch size for MODIS is 4x1, for Landsat 7 is 1x1, for Sentinel-1 is 8x1, for Sentinel-2 is 1x2, and for ALOS is 2x1. That is, we can observe that spatial patching leans toward higher resolution (i.e. small or no patching), while temporal aggregation within tokens is sometimes preferred (Sentinel-1, MODIS).

Table 3: Impact on **Accuracy** of data augmentation on training individual satellites. Columns show performance (i) with no data augmentation; (ii) adopting rotation and flip, and (iii) adding temporal masking with probability set as 50%.

Satellites	Data Augmentation		
	<i>none</i>	<i>rotation & flip</i>	<i>temporal masking</i>
Sentinel-1	51.0	50.66 (−0.34)	52.41 (1.41)
Sentinel-2	56.37	56.55 (0.17)	60.13 (3.75)
Landsat-7	54.25	52.56 (−1.69)	56.26 (2.01)
MODIS	45.23	44.55 (−0.67)	48.34 (3.12)
ALOS-2	28.63	23.13 (−5.5)	28.62 (−0.01)

Table 4: Validation, Test Accuracy and F1 score for best performing groups of satellites and sub-splits ($F1_r$, $F1_c$ and $F1_f$ denote *rare*, *common* and *frequent* classes respectively). Selection of best models based on validation accuracy.

Satellites	Validation					Test				
	Acc.	F1 Macro	$F1_r$	$F1_c$	$F1_f$	Acc.	F1 Macro	$F1_r$	$F1_c$	$F1_f$
s2	96.1	60.3	26.1	51.3	86.9	96.1	61.7	31.7	50.4	87.7
s1-s2	95.7	61.4	31.2	50.3	87.3	95.8	62.2	34.8	50.1	87.3
alos-modis-s2	96.0	61.4	30.4	51.8	86.7	96.2	62.1	30.0	52.1	88.3
alos-modis-s1-s2	95.6	61.1	32.5	50.0	86.2	95.7	61.2	31.7	50.6	86.3
17-alos-modis-s1-s2	95.0	59.9	32.5	47.4	85.1	95.2	59.3	30.7	47.1	85.1

6.3 Training data augmentation

Many image augmentation techniques in computer vision adopt image transformations that are based on human perception invariances Cubuk *et al.* (2019). However, in remote sensing, texture often carries high information content, despite being difficult for humans to perceive. Therefore initially we limit our augmentations to affine spatial transformations (rotation and flip) and temporal masking (similar to temporal dropout in Sainte Fare Garnot *et al.* (2022)). We explore three different data augmentation policies: (i) training with no data augmentation; (ii) training with rotation and flip; and (iii) temporal masking.

In Table 3 we show the performance of different satellites with and without augmentations. Spatial augmentation usually helped, and we observed improvements of 1% to 3% with temporal masking, except for Sentinel-2 and MODIS. MODIS has the longest time series with high redundancy, which is why we hypothesize the temporal augmentation was not helpful. Sentinel-2 on the other hand has the highest amount of missing data. These results were surprising and we are continuing to investigate it.

6.4 Fusing multiple modalities

In order to maximize the benefits of all modalities available, we explored different approaches for multimodal fusion. The optimal patch size derived for each individual satellite in the previous section was used here when combining multiple satellites.

Table 4 presents the best selected configuration as we increase the number of satellites. The selection was done based on the validation F1 macro score. We also present the sub-split and test metrics. Interestingly, the best validation accuracy and F1 scores are obtained using 2 or 3 satellite data sources. As expected, we observe significant differences between rare, common, and frequent classes, ranging from 26.1% $F1_r$ to 87.3% $F1_f$, with $F1_c$ falling between the two. An important challenge for future research could be to improve $F1_r$ and $F1_c$.

We also evaluated the performance of non-transformer models commonly used in remote sensing; namely a fully connected network and a random forest. Those models were optimized using AutoML on the cases of a single satellite and all satellites. The best test F1 Macro was achieved by the fully connected network, with a value of 51.8%. The random forest showed a best value of 41.6%.

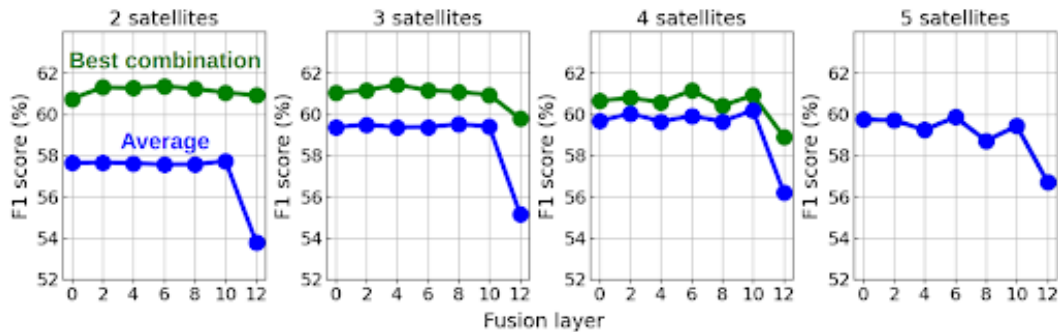


Figure 5: Performance for different fusion layers. The green line shows the top performing combination of satellites, and the blue line the average performance across all combinations of satellites.

6.5 Early vs. late fusion

To identify a good generic layer at which to fuse modalities, we evaluated the performance of all satellite combinations when fusing modalities at different transformer layers. After averaging across all modality combinations, Figure 5 illustrates the performance of the best satellite combination and the average across all combinations.

We observe that optimal performance is typically achieved using mid fusion. The worst performance is always observed when fusing in the last layer, suggesting that the simple fusion of independent models is not an efficient approach to combine multiple satellites. Instead, the different transformer backbones should be allowed to exchange information earlier in the stack to maximize the distillation of satellite information.

7 Conclusion

We present the *Planted* dataset for global planted forest and tree crop recognition from multi-satellite time series. This dataset addresses a critical need in the sustainability space (the delineation of planted forests), and further offers AI researchers a diverse and challenging problem.

This dataset poses challenging questions for exploration: How can we efficiently fuse information from multiple satellite sources? What are the most effective pretraining strategies for multimodal remote sensing tasks? What are the optimal methods for handling dataset imbalances?

We present initial baseline results evaluating single-modality time-series models as well as multimodal fusion. We hope these results can serve as a benchmark for the community, and that users of this dataset can build upon our methods to develop models that transfer well across geographies, satellite modalities and time. We hope this helps the global forestry community to develop comprehensive, accurate, planet-scale forest monitoring.

Acknowledgments

We would like to thank Nancy Harris, Liz Goldman and Sarah Carter from the World Resources Institute for advice regarding the SDPT data. We thank Ross Goroshin for designing initial figures for MODIS temporal signatures and Vishal Batchu for advising us on Google Earth Engine pipelines.

Data sources acknowledgments: Landsat 7 image courtesy of the U.S. Geological Survey. MODIS data courtesy of the U.S. Geological Survey Vermote (2021). Sentinel-1 and Sentinel-2 data courtesy of the ESA Copernicus program. Contains modified Copernicus Sentinel data 2015-2017. ALOS-2 PALSAR-2 data courtesy of JAXA (Japan Aerospace Exploration Agency). Aggregated and harmonized forest plantations labels data courtesy of Nancy Harris, Elizabeth Goldman and Samantha Gibbs, "Spatial Database of Planted Trees (SDPT Version 1.0)", World Resources Institute, 2019 Harris *et al.* (2019).

References

- Alemohammad, Hamed, & Booth, Kevin. 2020. LandCoverNet: A global benchmark land cover classification training dataset. *arXiv:2012.03111*.
- Arnab, Anurag, Dehghani, Mostafa, Heigold, Georg, Sun, Chen, Lučić, Mario, & Schmid, Cordelia. 2021. ViViT: A Video Vision Transformer. *In: International Conference on Computer Vision (ICCV)*.
- Brown, Christopher F, Brumby, Steven P, Guzder-Williams, Brookie, Birch, Tanya, Hyde, Samantha Brooks, Mazzariello, Joseph, Czerwinski, Wanda, Pasquarella, Valerie J, Haertel, Robert, Ilyushchenko, Simon, Schwehr, Kurt, Weisse, Mikaela, Stolle, Fred, Hanson, Craig, Guinan, Oliver, Moore, Rebecca, & Tait, Alexander M. 2022. Dynamic World, Near real-time global 10 m land use land cover mapping. *Scientific Data*, **9**(1), 1–17.
- Cha, Miriam, Huang, Kuan Wei, Schmidt, Morgan, Angelides, Gregory, Hamilton, Mark, Goldberg, Sam, Cabrera, Armando, Isola, Phillip, Perron, Taylor, Freeman, Bill, Lin, Yen-Chen, Swenson, Brandon, & Piou, Jean. 2022. MultiEarth 2022 – Multimodal Learning for Earth and Environment Workshop and Challenge. *arXiv:2204.07649*.
- Christie, Gordon, Fendley, Neil, Wilson, James, & Mukherjee, Ryan. 2018. Functional Map of the World. *2018 IEEE/CVF Conference on Computer Vision and Pattern Recognition*, Jun.
- Cubuk, Ekin D., Zoph, Barret, Mane, Dandelion, Vasudevan, Vijay, & Le, Quoc V. 2019 (June). AutoAugment: Learning Augmentation Strategies From Data. *In: Computer Vision and Pattern Recognition (CVPR)*.
- Elachi, Charles, & Van Zyl, Jakob J. 2006. *Introduction to the physics and techniques of remote sensing*. Vol. 28. John Wiley & Sons.
- Georgescu, Mariana-Iuliana, Fonseca, Eduardo, Ionescu, Radu Tudor, Lucic, Mario, Schmid, Cordelia, & Arnab, Anurag. 2022. Audiovisual Masked Autoencoders. *arXiv preprint arXiv:2212.05922*.
- Gong, Yuan, Chung, Yu-An, & Glass, James. 2021. Ast: Audio spectrogram transformer. *In: Interspeech*.
- Gorelick, Noel, Hancher, Matt, Dixon, Mike, Ilyushchenko, Simon, Thau, David, & Moore, Rebecca. 2017. Google Earth Engine: Planetary-scale geospatial analysis for everyone. *Remote Sensing of Environment*, **202**, 18–27.
- Hansen, M.C., Potapov, Peter, Moore, Rebecca, Hancher, M, Turubanova, Svetlana, Tyukavina, Alexandra, Thau, D, Stehman, Stephen, Goetz, Scott, Loveland, Thomas, Kommareddy, Anil, Egorov, Alexey, Chini, L, Justice, C.O., & Townshend, J. 2013. High-Resolution Global Maps of 21st-Century Forest Cover Change. *Science (New York, N.Y.)*, **342**(11), 850–853.
- Harris, Nancy, Dow Goldman, Elizabeth, & Gibbes, Samantha. 2019. *Spatial Database of Planted Trees (sdpt version 1.0)*. <https://files.wri.org/d8/s3fs-public/spatial-database-planted-trees.pdf>. Accessed: 2022-12-8.
- Helber, Patrick, Bischke, Benjamin, Dengel, Andreas, & Borth, Damian. 2019. EuroSAT: A Novel Dataset and Deep Learning Benchmark for Land Use and Land Cover Classification. *IEEE Journal of Selected Topics in Applied Earth Observations and Remote Sensing*, **12**(7), 2217–2226.
- Jaegle, Andrew, Gimeno, Felix, Brock, Andy, Vinyals, Oriol, Zisserman, Andrew, & Carreira, Joao. 2021. Perceiver: General perception with iterative attention. *In: International Conference on Machine Learning (ICML)*.
- Karpathy, Andrej, Toderici, George, Shetty, Sanketh, Leung, Thomas, Sukthankar, Rahul, & Fei-Fei, Li. 2014. Large-scale video classification with convolutional neural networks. *In: Computer Vision and Pattern Recognition (CVPR)*.

- Kolesnikov, Alexander, Dosovitskiy, Alexey, Weissenborn, Dirk, Heigold, Georg, Uszkoreit, Jakob, Beyer, Lucas, Minderer, Matthias, Dehghani, Mostafa, Houlsby, Neil, Gelly, Sylvain, Unterthiner, Thomas, & Zhai, Xiaohua. 2021. An Image is Worth 16x16 Words: Transformers for Image Recognition at Scale. *In: International Conference on Learning Representations (ICLR)*.
- Li, Guang, Zhu, Linchao, Liu, Ping, & Yang, Yi. 2019. Entangled transformer for image captioning. *In: International Conference on Computer Vision (ICCV)*.
- Lu, Jiasen, Batra, Dhruv, Parikh, Devi, & Lee, Stefan. 2019. Vilbert: Pretraining task-agnostic visiolinguistic representations for vision-and-language tasks. *Advances in Neural Information Processing Systems (NeurIPS)*.
- Nagrani, Arsha, Yang, Shan, Arnab, Anurag, Jansen, Aren, Schmid, Cordelia, & Sun, Chen. 2021. Attention bottlenecks for multimodal fusion. *Advances in Neural Information Processing Systems (NeurIPS)*.
- Papathanassiou, KP, Cloude, SR, Quiñones, MJ, Hoekman, D, Ferro-Famil, L, Goodenough, D, Chen, H, Tebaldini, S, Neumann, M, Ulander, LMH, & Soja, MJ. 2021. Forest applications. *Polarimetric Synthetic Aperture Radar: Principles and Application*, 59–117.
- Potapov, Peter, Li, Xinyuan, Hernandez-Serna, Andres, Tyukavina, Alexandra, Hansen, Matthew C, Kommareddy, Anil, Pickens, Amy, Turubanova, Svetlana, Tang, Hao, Silva, Carlos Edibaldo, *et al.* 2021. Mapping global forest canopy height through integration of GEDI and Landsat data. *Remote Sensing of Environment*, **253**, 112165.
- Programme, United Nations Environment. 2022. *Making good on the Glasgow Climate Pact: a call to action to achieve one gigaton of emissions reductions from forests by 2025*.
- Reiersen, Gyri, Dao, David, Lütjens, Björn, Klemmer, Konstantin, Amara, Kenza, Steinegger, Attila, Zhang, Ce, & Zhu, Xiaoxiang. 2022. ReforesTree: A Dataset for Estimating Tropical Forest Carbon Stock with Deep Learning and Aerial Imagery. *In: AAAI Conference on Artificial Intelligence*.
- Ronneberger, Olaf, Fischer, Philipp, & Brox, Thomas. 2015. U-Net: Convolutional Networks for Biomedical Image Segmentation. *Medical Image Computing and Computer-Assisted Intervention (MICCAI)*.
- Sainte Fare Garnot, Vivien, Landrieu, Loic, & Chehata, Nesrine. 2022. Multi-modal temporal attention models for crop mapping from satellite time series. *ISPRS Journal of Photogrammetry and Remote Sensing*, **187**(May), 294–305.
- Schmitt, Michael, Hughes, Lloyd Haydn, & Zhu, Xiao Xiang. 2018. The SEN1-2 dataset for deep learning in SAR-optical data fusion. *arXiv:1807.01569*.
- Schulz, Christian, Ahlswede, Steve, Gava, Christiano, Helber, Patrick, Bischke, Benjamin, Arias, Florencia, Förster, Michael, Hees, Jörn, Demir, Begüm, & Kleinschmit, Birgit. 2022. *TreeSatAI Benchmark Archive for deep learning in forest applications*.
- Simonyan, Karen, & Zisserman, Andrew. 2014. Two-stream convolutional networks for action recognition in videos. *Advances in Neural Information Processing Systems (NeurIPS)*.
- Sumbul, G., Charfuelan, M., Demir, B., & Markl, V. 2019 (Jul). BigEarthNet: A Large-Scale Benchmark Archive For Remote Sensing Image Understanding. *Pages 5901–5904 of: IEEE International Conference on Geoscience and Remote Sensing Symposium*.
- Tolan, Jamie, Yang, Hung-I, Nosarzewski, Ben, Couairon, Guillaume, Vo, Huy, Brandt, John, Spore, Justine, Majumdar, Sayantan, Haziza, Daniel, Vamaraju, Janaki, *et al.* 2023. Sub-meter resolution canopy height maps using self-supervised learning and a vision transformer trained on Aerial and GEDI Lidar. *arXiv:2304.07213*.
- Tseng, Gabriel, Zvonkov, Ivan, Nakalembe, Catherine Lilian, & Kerner, Hannah. 2021. CropHarvest: A global dataset for crop-type classification. *In: Neural Information Processing Systems Datasets and Benchmarks Track*.

- Tucker, Compton, Brandt, Martin, Hiernaux, Pierre, Kariryaa, Ankit, Rasmussen, Kjeld, Small, Jennifer, Igel, Christian, Reiner, Florian, Melocik, Katherine, Meyer, Jesse, Sinno, Scott, Romero, Eric, Glennie, Erin, Fitts, Yasmin, Morin, August, Pinzon, Jorge, McClain, Devin, Morin, Paul, Porter, Claire, Loeffler, Shane, Kergoat, Laurent, Issoufou, Bil-Assanou, Savadogo, Patrice, Wigneron, Jean-Pierre, Poulter, Benjamin, Ciaï, Philippe, Kaufmann, Robert, Myneni, Ranga, Saatchi, Sassan, & Fensholt, Rasmus. 2023. Sub-continental-scale carbon stocks of individual trees in African drylands. *Nature*, **615**(7950), 80–86.
- Vaswani, Ashish, Shazeer, Noam, Parmar, Niki, Uszkoreit, Jakob, Jones, Llion, Gomez, Aidan N, Kaiser, Łukasz, & Polosukhin, Illia. 2017. Attention is all you need. *Advances in Neural Information Processing Systems (NeurIPS)*, **30**.
- Vermote, E. 2021. *MODIS/Terra Surface Reflectance 8-Day L3 Global 500m SIN Grid V061. 2021, distributed by NASA EOSDIS Land Processes DAAC*. <https://doi.org/10.5067/MODIS/MOD09A1.061>. Accessed 2023-05-31.
- Wang, Peng, Yang, An, Men, Rui, Lin, Junyang, Bai, Shuai, Li, Zhikang, Ma, Jianxin, Zhou, Chang, Zhou, Jingren, & Yang, Hongxia. 2022. Ofa: Unifying architectures, tasks, and modalities through a simple sequence-to-sequence learning framework. *In: International Conference on Machine Learning (ICML)*.
- Yang, Yi, & Newsam, Shawn. 2010. Bag-of-visual-words and spatial extensions for land-use classification. *Page 270 of: Proceedings of the 18th SIGSPATIAL International Conference on Advances in Geographic Information Systems - GIS '10*. New York, USA: ACM Press.
- Zhu, Xiao Xiang, Hu, Jingliang, Qiu, Chunping, Shi, Yilei, Kang, Jian, Mou, Lichao, Bagheri, Hossein, Haberle, Matthias, Hua, Yuansheng, Huang, Rong, Hughes, Lloyd, Li, Hao, Sun, Yao, Zhang, Guichen, Han, Shiyao, Schmitt, Michael, & Wang, Yuanyuan. 2020. So2Sat LCZ42: A Benchmark Data Set for the Classification of Global Local Climate Zones. *IEEE Geoscience and Remote Sensing Magazine*, **8**(3), 76–89.

A Satellite data details

This section describes the used satellite data in more detail and includes tables of data bands included in the *Planted* dataset.

Sentinel-1 (S1) satellites carry a Synthetic Aperture Radar (SAR) at C-band frequency (center wavelength of 5.54 cm (5.4 GHz), with a bandwidth of 100 MHz). It images land and ice surfaces of the Earth between -79 and +82 degrees latitude. It can send and receive at vertical and horizontal polarizations, though we include data only for the more common VV and VH combinations (vertical transmit, and vertical and horizontal receive). Currently there is only a single satellite in operation (Sentinel-1A, launched in 2014) with a revisit time on each point on Earth of 12 days. Sentinel-1B, launched in 2016 had a malfunction and provided data only till Dec 2021 (in this time range the revisit time for both satellites was 6 days). Sentinel-1C is expected to be launched in 2023. We extract the backscatter at VV and HV polarizations, which are already converted to decibel (dB). Additional pre-processing within Google Earth Engine includes thermal noise removal, radiometric calibration, and terrain correction. SAR data is very sensitive to the incidence angle at the surface, and therefore we also include the used incidence angle with respect to reference Earth ellipsoid (Table 5).

Table 5: Included bands from Sentinel-1.

Index	Bands	Description
0	VV	Vertically polarized transmit and receive, in dB
1	VH	Vertically polarized transmit and horizontally polarized receive, in dB
2	angle	Incidence angle

Sentinel-2 (S2) The satellite constellation of ESA’s Copernicus program contains of 2 satellites with medium-resolution multi-spectral imagers (as of 2023): Sentinel-2A was launched in June 2015 and Sentinel-2B in March 2017 (Sentinel-2C expected to launch in 2024, and Sentinel-2D in 2025). Each satellite revisits the same point on Earth every 10 days. Since they operate at an offset, they image the target Earth regions (land and coastal, between -56 and 83 degrees latitude) every 5 days at the equator (and with higher frequency towards the poles). Sentinel-2’s are polar-orbiting sun-synchronous (always imaging the Earth at 10:30 local time) with a ground swath of 290 km. S2 is a multi-spectral instrument, measuring reflectance of sun’s illumination from the Earth in 13 bands with different center frequencies (between 0.442 μm and 2.186 μm , bandwidths (0.02 μm to 0.185 μm) and pixel resolutions (10 m to 60 m). The list of bands used in *Planted* dataset is presented in Table 6. The bands B1, B9 and B10 are used mostly for clouds/atmosphere. B2-B4 are blue, green, red bands. B5-B8A are vegetation red edge and near-infra-red (NIR) bands sensitive to fine vegetation characteristics. Finally, longer wavelength bands B11-B12 are short-wave infrared (SWIR) bands with sensitivity to moisture and fine structural properties.

Table 6: Included bands from Sentinel-2 (reference numbers from Sentinel-2A).

Index	Band	Wavelength	Bandwidth	Resolution	Description
0	B2	492.4 nm	66 nm	10 m	Blue
1	B3	559.8 nm	36 nm	10 m	Green
2	B4	664.6 nm	31 nm	10 m	Red
3	B5	704.1 nm	15 nm	20 m	Vegetation red edge 1
4	B6	740.5 nm	15 nm	20 m	Vegetation red edge 2
5	B7	782.8 nm	20 nm	20 m	Vegetation red edge 3
6	B8	832.8 nm	106 nm	10 m	Near infrared (NIR)
7	B8A	864.7 nm	21 nm	20 m	Narrow NIR
8	B11	1612.7 nm	91 nm	20 m	Short wave infrared (SWIR) 1
9	B12	2202.4 nm	175 nm	20 m	Short wave infrared (SWIR) 2

Landsat-7 (L7) the seventh satellite of NOAA and NASA’s Landsat program, was launched in April 1999 and was operational far beyond the envisioned five year mission duration, and was

decommissioned only in 2021. Similar to Sentinel-2 it has a polar, sun-synchronous orbit, with equatorial crossing time of about 10:00 am, and with a 16 days revisit time needed to scan the entire Earth. The main imaging instrument on board of Landsat 7 is the Enhanced Thematic Mapper Plus (ETM+), providing 8 bands. For the *Planted* dataset we keep only the 30m resolution bands (Table 7, dropping the panchromatic (B8) and the thermal (B6) bands.

Table 7: Included bands from Landsat-7.

Index	Band	Wavelength	Bandwidth	Resolution	Description
0	B1	485 nm	70 nm	30 m	Blue
1	B2	560 nm	80 nm	30 m	Green
2	B3	660 nm	60 nm	30 m	Red
3	B4	835 nm	130 nm	30 m	Near infrared (NIR)
4	B5	1650 nm	200 nm	30 m	Short wave infrared (SWIR) 1
5	B7	2215 nm	270 nm	30 m	Short wave infrared (SWIR) 2

ALOS-2 carries the PALSAR-2 SAR instrument at L-band frequency (center wavelength: 22.9 cm, 1.2 GHz; bandwidth: 14-84 MHz). It is the third satellite with an L-band SAR from the Japan Aerospace Exploration Agency (JAXA): first was JERS-1 launched in 1992, then ALOS/PALSAR launched in 2006, while ALOS-2/PALSAR-2 was launched in 2014. Due to larger wavelength than C-band from Sentinel-1, ALOS electromagnetic waves can penetrate deeper into the forest canopy and are more sensitive to tree trunks and branches, and can get a significant ground-trunk double-bounce scattering contribution. Similar to Sentinel-1, it is a fully polarimetric SAR sensor, though the majority of data is available in HH and HV combination. We use the pre-processed yearly mosaics as they are provided by Google Earth Engine. The HH and HV backscatter magnitudes (Table 8 are represented by 16-bit digital numbers (DN) and they can be converted to backscatter values in decibels (dB) via:

$$\gamma = 10 \log_{10}(\text{DN}^2) - 83.0 \text{ dB}$$

Table 8: Included bands from ALOS-2 PALSAR-2.

Index	Bands	Description
0	HH	Horizontally polarized transmit and receive
1	HV	Horizontally polarized transmit and vertically polarized receive
2	angle	Incidence angle

MODIS (Moderate Resolution Imaging Spectrometer) is a multi-spectral imaging instrument on board of Terra and Aqua satellites. It has much lower spatial resolution (250m to 1km) than Sentinel-2 or Landsat-7, but it images the Earth (land, ocean, and atmosphere) in more frequency bands (36), and at more frequent intervals (every 1-2 days). Terra was launched in December 1999, and Aqua was launched in May 2002. Both fly on near-polar, sun-synchronous, circular orbits. Of importance for forest monitoring are especially the first seven bands, while others are used for monitoring the ocean and the atmosphere.

Table 9: Included bands from MODIS Terra/Aqua satellites.

Index	Band	Wavelength	Bandwidth	Resolution	Description
0	B01	645 nm	50 nm	250 m	Red
1	B02	858 nm	35 nm	250 m	Near infrared (NIR)
2	B03	469 nm	20 nm	500 m	Blue
3	B04	555 nm	20 nm	500 m	Green
4	B05	1240 nm	20 nm	500 m	Short wave infrared (SWIR)
5	B06	1640 nm	24 nm	500 m	Short wave infrared (SWIR)
6	B07	2130 nm	50 nm	500 m	Short wave infrared (SWIR)

A.1 Missing data and samples availability per satellite

Despite temporal aggregation of satellite observations often some data still remains missing. Figure 6 outlines the percentages of missing data across time. ALOS data, partially due to yearly aggregation is nearly always available to 100%. MODIS data is usually available (99.8%). Landsat-7 data is missing in about 8.6% of data, as does Sentinel-2. Sentinel-1 misses 6.9%. Since Sentinel-1 and -2 were launched the latest, it takes time till the data becomes stable and well calibrated. Therefore we see initially large amounts of missing data in early 2016 (31.4% for S1 and 21.7% for S2) which falls over the 2 year range to 0% for S1 and 2.5% for S2.

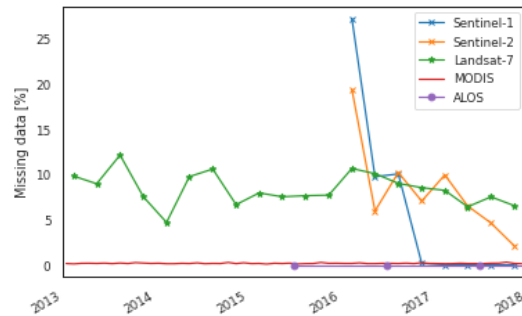


Figure 6: Percentages of missing data over time per satellite (based on 200,000 random examples from the train split).

B Labels data details

Table 12 presents the distribution of species across train, validation and test splits. It also denotes ratio of train examples to the total number of examples; and the frequency annotation based on the available number of examples for the given species within the dataset.

Each of the 64 label categories has a unique species name and common name. Next, we can assign each species to either timber or tree crop class, to being conifer or broad-leaf trees, to be evergreen or deciduous (some species can be both, in dependence of climate conditions), and to have soft or hard wood. Table 13 lists all correspondences. If a specific value was not provided, we mark it as *Unknown*.

Table 10: Recognized tree species and common names for the given genera.

Genus	Tree species	Common names
Abies	Abies sachalinensis	Sakhalin Fir
Acacia	Acacia melanoxylon	Acacia/Wattle, Australian Blackwood
Acer	Acer pictum	Mono Maple
Alnus		Alder
Anacardium	Anacardium occidentale	Cashew
Araucaria		Monkey Puzzle
Areca		Areca Palm
Betula	Betula pendula	East Asian White Birch
Callitris		Cypress Pine
Camellia	Thea sinensis	Tea
Castanea	Castanea crenata	Korean Chestnut
Casuarina		Casuarina
Cedrus		Cedar
Citrus		Orange
Cocos	Cocos nucifera	Coconut Palm
Coffea		Coffee
Cornus	Cornus controversa	Wedding Cake
Cryptomeria	Cryptomeria japonica	Japanese Red Cedar
Dendropanax	Dendropanax morbiferus	Korean Dendropanax
Elaeis	Elaeis guineensis	Oil Palm
Eucalyptus	Eucalyptus globulus, Eucalyptus nitens	Eucalyptus, Tasmanian Bluegum, Shining Gum
Fraxinus	Fraxinus rhynchophylla	East Asian Ash
Ginkgo	Ginkgo biloba	Ginkgo
Gliricidia		Gliricidia
Grevillea		Grevillea
Hevea	Hevea brasiliensis	Rubber
Jacaranda		Jacaranda
Larix		Larch
Lithocarpus	Pasania edulis	Japanese Stone Oak
Machilus	Machilus thunbergii	Japanese Bay Tree
Malus	Malus pumila	Apple
Mangifera		Mango
Morus		Mulberry
Musa		Banana
Picea	Picea glehnii, Picea jezoensis, Picea mariana	Spruce, Sakhalin Spruce, Jezo Spruce, Black Spruce
Pinus	Pinus densiflora, Pinus thunbergii, Pinus koraiensis, Pinus rigida, Pinus elliottii, Pinus taeda, Pinus echinata, Pinus radiata	Red Pine, Black Pine, Korean Pine, Pitch Pine, Slash Pine, Loblolly Pine, Shortleaf Pine, Pine, Monterey Pine
Populus		Poplar
Prunus	Prunus serrulata, Prunus dulcis	Japanese Flowering Cherry, Almond
Pseudotsuga	Pseudotsuga menziesii	Douglas Fir
Pterocarpus		Padauk
Quercus	Quercus acutissima, Quercus variabilis	Oak, Sawtooth Oak, Chinese Cork Oak
Robinia	Robinia pseudoacacia	Black Locust
Shorea	Shorea robusta	Sal
Tectona		Teak
Theobroma	Theobroma cacao	Cacao
Zelkova	Zelkova serrata	Sawleaf Zelkova

Table 11: Distribution of genus labels across training splits with frequency annotation (columns: genus, total number of examples, train/validation/test examples, frequency annotation of the given genera within the dataset).

	Tree genus	Total	Train	Validation	Test	Frequency
1	Pinus	929381 (41.037%)	735144	94916	99321	frequent
2	Elaeis	466895 (20.616%)	369606	49603	47686	frequent
3	Eucalyptus	271718 (11.998%)	212349	27706	31663	frequent
4	Larix	196918 (8.695%)	147690	29215	20013	frequent
5	Abies	57864 (2.555%)	40703	8982	8179	frequent
6	Tectona	43840 (1.936%)	26278	11846	5716	frequent
7	Shorea	42267 (1.866%)	28532	7772	5963	frequent
8	Castanea	38537 (1.702%)	20344	9964	8229	frequent
9	Pseudotsuga	36350 (1.605%)	28704	3690	3956	frequent
10	Populus	25159 (1.111%)	18518	3052	3589	frequent
11	Acacia	24885 (1.099%)	16645	5740	2500	frequent
12	Morus	19921 (0.880%)	13717	4093	2111	frequent
13	Robinia	19912 (0.879%)	14319	3400	2193	frequent
14	Picea	17893 (0.790%)	13469	1878	2546	frequent
15	Areca	11853 (0.523%)	8385	2930	538	frequent
16	Camellia	11301 (0.499%)	7477	1153	2671	frequent
17	Betula	10387 (0.459%)	7305	2043	1039	frequent
18	Quercus	9904 (0.437%)	6790	2053	1061	common
19	Hevea	8450 (0.373%)	6506	848	1096	common
20	Cedrus	7357 (0.325%)	4822	1530	1005	common
21	Mangifera	2859 (0.126%)	1323	294	1242	common
22	Cocos	1964 (0.087%)	1216	204	544	common
23	Anacardium	1544 (0.068%)	772	498	274	common
24	Prunus	1287 (0.057%)	810	217	260	common
25	Zelkova	1098 (0.048%)	840	132	126	common
26	Alnus	862 (0.038%)	561	99	202	common
27	Acer	815 (0.036%)	630	90	95	common
28	Coffea	738 (0.033%)	420	80	238	common
29	Fraxinus	433 (0.019%)	314	44	75	common
30	Musa	364 (0.016%)	245	48	71	common
31	Casuarina	297 (0.013%)	223	36	38	common
32	Ginkgo	290 (0.013%)	190	54	46	common
33	Callitris	257 (0.011%)	166	39	52	common
34	Grevillea	229 (0.010%)	156	36	37	common
35	Lithocarpus	197 (0.009%)	122	37	38	rare
36	Dendropanax	136 (0.006%)	67	35	34	rare
37	Gliricidia	134 (0.006%)	46	36	52	rare
38	Machilus	124 (0.005%)	56	34	34	rare
39	Cryptomeria	112 (0.005%)	66	37	9	rare
40	Malus	52 (0.002%)	26	12	14	rare
41	Pterocarpus	39 (0.002%)	14	18	7	rare
42	Citrus	38 (0.002%)	12	14	12	rare
43	Jacaranda	31 (0.001%)	9	13	9	rare
44	Cornus	25 (0.001%)	8	7	10	rare
45	Araucaria	15 (0.001%)	5	5	5	rare
46	Theobroma	15 (0.001%)	6	4	5	rare

Table 12: Distribution of tree species labels across training splits with frequency annotation (columns: tree species, total number of examples, train/validation/test examples, frequency annotation of the given species within the dataset).

	Tree species	Total	Train	Validation	Test	Frequency
1	Elaeis guineensis	466895 (34.631%)	373074	47103	46718	frequent
2	Pinus taeda	205606 (15.250%)	164474	20571	20561	frequent
3	Pinus rigida	125575 (9.314%)	100230	12719	12626	frequent
4	Pinus koraiensis	99082 (7.349%)	79076	9969	10037	frequent
5	Pinus densiflora	67861 (5.033%)	54167	6811	6883	frequent
6	Abies sachalinensis	56038 (4.156%)	44690	5669	5679	frequent
7	Pinus elliotii	43072 (3.195%)	34406	4318	4348	frequent
8	Shorea robusta	42267 (3.135%)	33319	4408	4540	frequent
9	Castanea crenata	38537 (2.858%)	30569	4099	3869	frequent
10	Pseudotsuga menziesii	36350 (2.696%)	29059	3641	3650	frequent
11	Eucalyptus globulus	29643 (2.199%)	23661	2966	3016	frequent
12	Pinus radiata	24963 (1.852%)	19930	2516	2517	frequent
13	Robinia pseudoacacia	19912 (1.477%)	15743	2168	2001	frequent
14	Pinus thunbergii	18478 (1.371%)	14735	1893	1850	frequent
15	Pinus echinata	13532 (1.004%)	10803	1356	1373	frequent
16	Thea sinensis	11301 (0.838%)	8983	1155	1163	frequent
17	Betula pendula	10387 (0.770%)	8297	1043	1047	frequent
18	Hevea brasiliensis	8450 (0.627%)	6683	916	851	common
19	Picea glehnii	8263 (0.613%)	6589	840	834	common
20	Quercus acutissima	6961 (0.516%)	5551	713	697	common
21	Eucalyptus nitens	5630 (0.418%)	4477	571	582	common
22	Cocos nucifera	1964 (0.146%)	1555	200	209	common
23	Anacardium occidentale	1544 (0.115%)	1208	178	158	common
24	Zelkova serrata	1098 (0.081%)	878	110	110	common
25	Acer pictum	815 (0.060%)	647	82	86	common
26	Prunus serrulata	653 (0.048%)	519	66	68	common
27	Prunus dulcis	634 (0.047%)	486	76	72	common
28	Picea jezoensis	622 (0.046%)	491	68	63	common
29	Quercus variabilis	597 (0.044%)	467	64	66	common
30	Fraxinus rhynchophylla	433 (0.032%)	345	44	44	common
31	Ginkgo biloba	290 (0.022%)	218	34	38	common
32	Pasania edulis	197 (0.015%)	122	35	40	rare
33	Dendropanax morbiferus	136 (0.010%)	67	34	35	rare
34	Machilus thunbergii	124 (0.009%)	58	36	30	rare
35	Cryptomeria japonica	112 (0.008%)	50	28	34	rare
36	Acacia melanoxylon	54 (0.004%)	24	13	17	rare
37	Malus pumila	52 (0.004%)	17	9	26	rare
38	Picea mariana	51 (0.004%)	17	22	12	rare
39	Cornus controversa	25 (0.002%)	10	8	7	rare
40	Theobroma cacao	15 (0.001%)	6	5	4	rare

Table 13: Planted trees traits (columns: common species name; official species name; whether it is a timber or tree crops plantation; whether those are conifer or broad leaf trees; whether evergreen or deciduous; and whether those trees are considered to have soft or hard wood).

	Common name	Species/genus name	timber / crops	confr / broadl	ever / dec	soft / hard
1	Oil Palm	Elaeis guineensis	Tree crops	Unknown	Unknown	Unknown
2	Pine	Pinus sp.	Planted forest	Conifer	Evergreen	Softwood
3	Eucalyptus	Eucalyptus sp.	Planted forest	Broadleaf	Evergreen	Hardwood
4	Loblolly Pine	Pinus taeda	Planted forest	Conifer	Evergreen	Softwood
5	Larch	Larix sp.	Planted forest	Conifer	Deciduous	Softwood
6	Pitch Pine	Pinus rigida	Planted forest	Conifer	Evergreen	Softwood
7	Korean Pine	Pinus koraiensis	Planted forest	Broadleaf	Evergreen	Softwood
8	Red Pine	Pinus densiflora	Planted forest	Conifer	Evergreen	Softwood
9	Sakhalin Fir	Abies sachalinensis	Planted forest	Conifer	Evergreen	Softwood
10	Teak	Tectona sp.	Planted forest	Broadleaf	Deciduous	Hardwood
11	Slash Pine	Pinus elliotii	Planted forest	Conifer	Evergreen	Softwood
12	Sal	Shorea robusta	Planted forest	Broadleaf	Evergr/Decid	Hardwood
13	Korean Chestnut	Castanea crenata	Tree crops	Unknown	Unknown	Unknown
14	Douglas Fir	Pseudotsuga menziesii	Planted forest	Conifer	Evergreen	Softwood
15	Tasmanian Bluegum	Eucalyptus globulus	Planted forest	Broadleaf	Evergreen	Hardwood
16	Poplar	Populus sp.	Planted forest	Broadleaf	Deciduous	Hardwood
17	Monterey Pine	Pinus radiata	Planted forest	Conifer	Evergreen	Softwood
18	Acacia/Wattle	Acacia sp.	Planted forest	Broadleaf	Deciduous	Hardwood
19	Mulberry	Morus sp.	Tree crops	Unknown	Unknown	Unknown
20	Black Locust	Robinia pseudoacacia	Planted forest	Broadleaf	Deciduous	Hardwood
21	Black Pine	Pinus thunbergii	Planted forest	Conifer	Evergreen	Softwood
22	Shortleaf Pine	Pinus echinata	Planted forest	Conifer	Evergreen	Softwood
23	Areca Palm	Areca sp.	Tree crops	Unknown	Unknown	Unknown
24	Tea	Thea sinensis	Tree crops	Unknown	Unknown	Unknown
25	East Asian White Birch	Betula pendula	Planted forest	Broadleaf	Deciduous	Unknown
26	Spruce	Picea sp.	Planted forest	Conifer	Evergreen	Softwood
27	Rubber	Hevea brasiliensis	Tree crops	Unknown	Unknown	Unknown
28	Sakhalin Spruce	Picea glehnii	Planted forest	Conifer	Evergreen	Softwood
29	Cedar	Cedrus sp.	Planted forest	Conifer	Evergreen	Softwood
30	Sawtooth Oak	Quercus acutissima	Planted forest	Broadleaf	Deciduous	Hardwood
31	Shining Gum	Eucalyptus nitens	Planted forest	Broadleaf	Evergreen	Hardwood
32	Mango	Mangifera sp.	Tree crops	Unknown	Unknown	Unknown
33	Oak	Quercus sp.	Planted forest	Broadleaf	Unknown	Hardwood
34	Coconut Palm	Cocos nucifera	Tree crops	Unknown	Unknown	Unknown
35	Fir	Abies sp.	Planted forest	Conifer	Evergreen	Softwood
36	Cashew	Anacardium occidentale	Tree crops	Unknown	Unknown	Unknown
37	Sawleaf Zelkova	Zelkova serrata	Planted forest	Broadleaf	Deciduous	Hardwood
38	Alder	Alnus sp.	Planted forest	Broadleaf	Deciduous	Hardwood
39	Mono Maple	Acer pictum	Planted forest	Broadleaf	Deciduous	Hardwood
40	Coffee	Coffea sp.	Tree crops	Unknown	Unknown	Unknown
41	Japanese Flowering Cherry	Prunus serrulata	Tree crops	Broadleaf	Deciduous	Hardwood
42	Almond	Prunus dulcis	Tree crops	Unknown	Unknown	Unknown
43	Jezo Spruce	Picea jezoensis	Planted forest	Conifer	Evergreen	Softwood
44	Chinese Cork Oak	Quercus variabilis	Tree crops	Broadleaf	Deciduous	Unknown
45	East Asian Ash	Fraxinus rhynchophylla	Planted forest	Broadleaf	Deciduous	Hardwood
46	Banana	Musa sp.	Tree crops	Unknown	Unknown	Unknown
47	Casuarina	Casuarina sp.	Planted forest	Broadleaf	Evergreen	Hardwood
48	Ginkgo	Ginkgo biloba	Tree crops	Unknown	Unknown	Unknown
49	Cypress Pine	Callitris sp.	Planted forest	Conifer	Evergreen	Softwood
50	Grevillea	Grevillea sp.	Planted forest	Broadleaf	Evergreen	Hardwood
51	Japanese Stone Oak	Pasania edulis	Tree crops	Broadleaf	Evergreen	Unknown
52	Korean Dendropanax	Dendropanax morbiferus	Tree crops	Unknown	Unknown	Unknown
53	Gliricidia	Gliricidia sp.	Tree crops	Unknown	Unknown	Unknown
54	Japanese Bay Tree	Machilus thunbergii	Planted forest	Broadleaf	Evergreen	Hardwood
55	Japanese Red Cedar	Cryptomeria japonica	Planted forest	Conifer	Evergreen	Softwood
56	Australian Blackwood	Acacia melanoxylon	Planted forest	Broadleaf	Evergreen	Hardwood
57	Apple	Malus pumila	Tree crops	Unknown	Unknown	Unknown
58	Black Spruce	Picea mariana	Planted forest	Conifer	Evergreen	Softwood
59	Padauk	Pterocarpus sp.	Planted forest	Broadleaf	Evergr/Decid	Hardwood
60	Orange	Citrus sp.	Tree crops	Unknown	Unknown	Unknown
61	Jacaranda	Jacaranda sp.	Planted forest	Broadleaf	Deciduous	Hardwood
62	Wedding Cake	Cornus controversa	Tree crops	Broadleaf	Deciduous	Unknown
63	Cacao	Theobroma cacao	Tree crops	Unknown	Unknown	Unknown
64	Monkey Puzzel	Araucaria sp.	Planted forest	Conifer	Evergreen	Softwood

Table 14: Default model and training configuration.

Name	Value
transformer layers	12
embedding size	192
number of heads	3
MLP size	768
optimizer	adamw
base learning rate	0.001
weight decay	0.0001
batch size	1024
training epochs	40
learning rte schedule	cosine decay
warmup	5 epochs
loss	softmax cross-entropy

C Model and training details

We used a standard vision transformer (ViT) architecture Kolesnikov *et al.* (2021) for single-modality results. The default configuration consisted of 12 transformer layers, each consisting of a multi-head (3) self-attention blocks and an MLP block with size 768, with layer normalization. The used embedding size is 192. Further model, optimizer and training configuration parametrs are shown in Table 14. For multi-temporal data, we extended the patching from spatial 2D to spatio-temporal 3D patches. For multi-modal experiments, to evaluate early, mid-, and late fusion, we followed Nagrani *et al.* (2021). We considered four training data augmentation approaches: none, rotation and flipping, temporal masking, and combination the last two.

D Additional experimental results

Figure 7 visualizes an ablation across different temporal masking probabilities for all individual satellite modalities. As can be observed, the best temporal masking probability for most satellites is between 30% and 50%, except for Alos data, where the best is at 10%. This result is intuitive, since Alos data has the fewest temporal samples and therefore relies a lot on all given data.

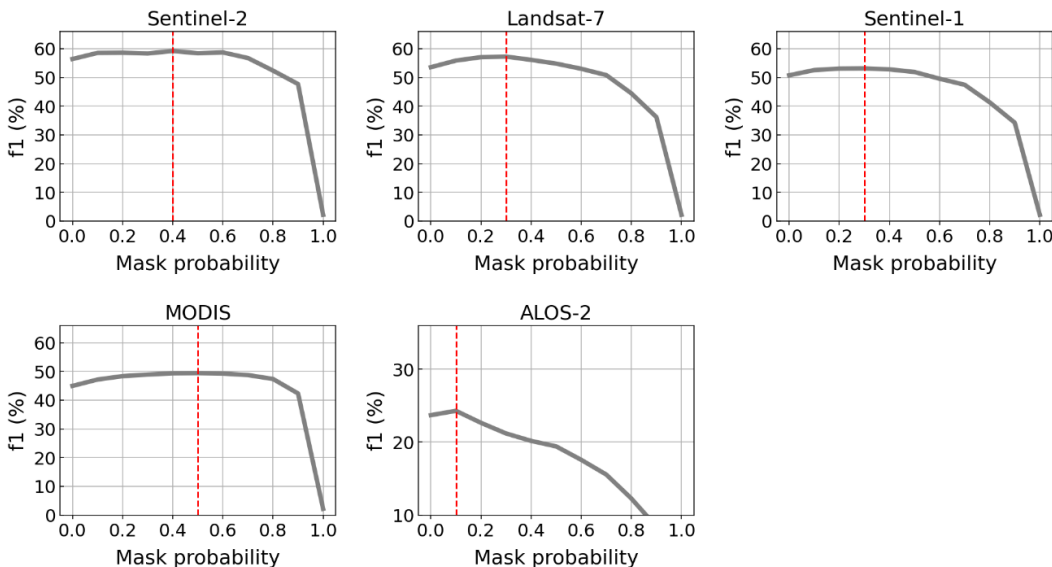


Figure 7: Validation F1 score over temporal masking probability for individual satellites.

Table 15: Baseline F1 metrics for random forests and neural networks. ($\mathbf{F1}_r$, $\mathbf{F1}_c$ and $\mathbf{F1}_f$ denote *rare*, *common* and *frequent* classes respectively). Optimal models were selected based on validation accuracy.

Satellites	Model	Validation				Test			
		F1 Macro	$\mathbf{F1}_r$	$\mathbf{F1}_c$	$\mathbf{F1}_f$	F1 Macro	$\mathbf{F1}_r$	$\mathbf{F1}_c$	$\mathbf{F1}_f$
s2	NN	49.5	17.1	34.1	79.4	50.6	20.4	34.7	79.7
s2	RF	30.7	1.5	9.1	63.9	32.0	4.2	11.5	63.5
s2-s1-modis-17-alos	NN	51.0	22.3	34.5	79.9	51.8	26.2	34.0	80.1
s2-s1-modis-17-alos	RF	39.7	5.4	24.9	70.0	41.6	7.9	25.4	72.8

Table 15 presents reference results using Random Forests or MLP models, where AutoML was used to optimize the configurations.